

Atom-probe analyses of nanodiamonds from Allende

Philipp R. HECK^{1,2*}, Frank J. STADERMANN^{3,4}, Dieter ISHEIM⁵, Orlando AUCIELLO^{6,7},
Tyrone L. DAULTON^{4,8}, Andrew M. DAVIS^{1,2,9,10}, Jeffrey W. ELAM¹¹, Christine FLOSS^{3,4},
Jon HILLER⁶, David J. LARSON¹², Josiah B. LEWIS^{3,4}, Anil MANE¹¹, Michael J. PELLIN^{2,6,9,10},
Michael R. SAVINA^{2,6}, David N. SEIDMAN⁵, and Thomas STEPHAN^{1,2,6,9}

¹Robert A. Pritzker Center for Meteoritics and Polar Studies, The Field Museum, Chicago, Illinois, USA

²Chicago Center for Cosmochemistry, The University of Chicago, Chicago, Illinois, USA

³Laboratory for Space Sciences, St. Louis, Missouri, USA

⁴Physics Department, Washington University, St. Louis, Missouri, USA

⁵Northwestern University Center for Atom-Probe Tomography, Department of Materials Science & Engineering,
Northwestern University, Evanston, Illinois, USA

⁶Materials Science Division, Argonne National Laboratory, Argonne, Illinois, USA

⁷Department of Materials Science and Engineering and Department of Bioengineering, University of Texas-Dallas,
Richardson, Texas, USA

⁸Center for Materials Innovation, Washington University, St. Louis, Missouri, USA

⁹Department of the Geophysical Sciences, The University of Chicago, Chicago, Illinois, USA

¹⁰Enrico Fermi Institute, The University of Chicago, Chicago, Illinois, USA

¹¹Energy Systems Division, Argonne National Laboratory, Argonne, Illinois, USA

¹²Cameca Instruments, Inc., Madison, Wisconsin, USA

*Corresponding author. E-mail: prheck@fieldmuseum.org

(Received 28 May 2013; revision accepted 27 December 2013)

Abstract—Atom-probe tomography (APT) is currently the only analytical technique that, due to its spatial resolution and detection efficiency, has the potential to measure the carbon isotope ratios of individual nanodiamonds. We describe three different sample preparation protocols that we developed for the APT analysis of meteoritic nanodiamonds at sub-nm resolution and present carbon isotope peak ratios of meteoritic and synthetic nanodiamonds. The results demonstrate an instrumental bias associated with APT that needs to be quantified and corrected to obtain accurate isotope ratios. After this correction is applied, this technique should allow determination of the distribution of ¹²C/¹³C ratios in individual diamond grains, solving the decades-old question of the origin of meteoritic nanodiamonds: what fraction, if any, formed in the solar system and in presolar environments? Furthermore, APT could help us identify the stellar sources of any presolar nanodiamonds that are detected.

INTRODUCTION

The origin of meteoritic nanodiamonds is still a mystery 26 yr after their discovery. Systematic bulk analyses of different separates from carbonaceous chondrites have shown that nanodiamond-bearing acid residues contain the carrier of the highly anomalous xenon isotope component Xe-HL (Lewis et al. 1987). Xe-HL is enriched in the two lightest xenon isotopes, ¹²⁴Xe and ¹²⁶Xe, both produced in the *p*-process, and also in the two heaviest isotopes, ¹³⁴Xe and ¹³⁶Xe, produced in the

r-process. Additionally, the same nanodiamond-rich separates contain small anomalies in the *r*-process nuclides ¹¹⁰Pd, ¹²⁸Te, and ¹³⁰Te (Richter et al. 1998; Maas et al. 2001) and in the *r,s*-process nuclide ¹³⁷Ba (Lewis et al. 1991). These *p*- and *r*-process anomalies can only be explained by nucleosynthetic processes that are thought to occur in supernovae. The abundance of these trapped nuclides is relatively low, and only a small fraction of the nanodiamond population can carry these anomalies. For instance, on average, only one of a million meteoritic diamonds contains a single trapped

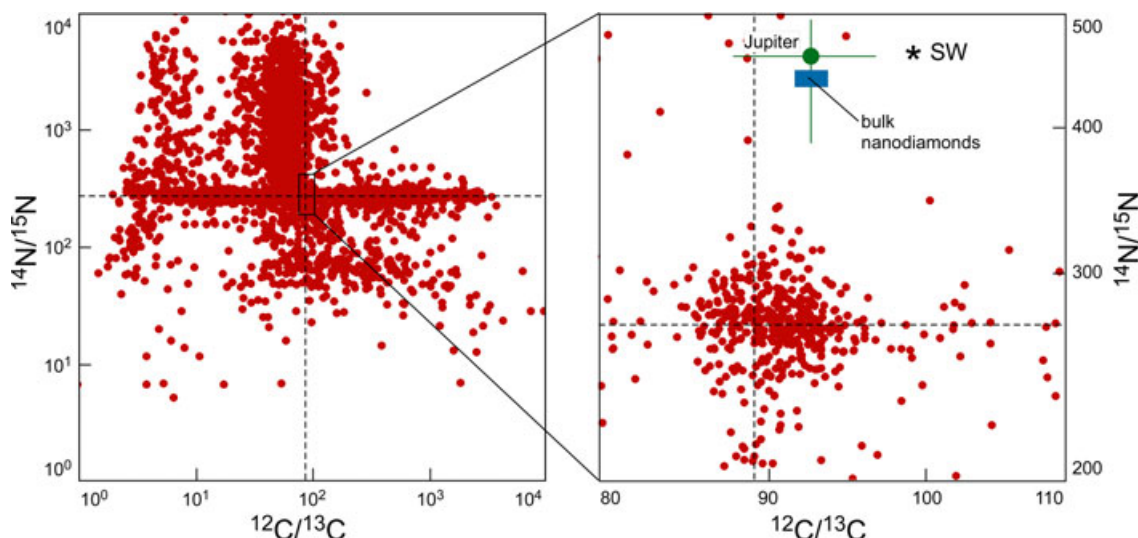


Fig. 1. Range of carbon and nitrogen isotopic compositions in bulk analyses of nanodiamond-containing acid residues (blue rectangle; data from Russell et al. 1996) compared with solar wind—SW; Marty et al. (2011), Jupiter (Owen et al. 2001; Atreya et al. 2003), and individual presolar silicon carbide and graphite grains (red dots; data from Presolar Grain Database; Hynes and Gygard 2009). Dashed lines are the terrestrial carbon standard (Vienna-PDB) and terrestrial air nitrogen isotope ratios (Coplen et al. 2002). Error bars are shown if larger than the symbol size.

xenon atom (for a review, see Daulton 2006); however, more diamonds contain anomalous neon and helium (Huss and Lewis 1994). As a solar system origin of these anomalies can be clearly excluded, meteoritic nanodiamonds have been classified as presolar.

A recent scanning transmission electron microscopy study showed that meteoritic nanodiamond-bearing acid residues also contain an sp^2 carbon phase resembling glassy carbon (Stroud et al. 2011). This two-phase mixture has been explained by the transformation of organic carbon to nanodiamonds and glassy carbon by supernova shockwaves in the interstellar medium (ISM). It is, moreover, consistent with the astronomically observed 2175 Å extinction feature in the ISM (Stroud et al. 2011). The presolar isotopic anomalies could be carried by the nanodiamonds, by the glassy carbon, or by both. Earlier high-resolution (HR)-TEM studies have, however, demonstrated that the growth and defect atomic microstructures of the majority of meteoritic nanodiamonds from Allende and Murchison are inconsistent with shock-transformation processes and instead are consistent with vapor condensation occurring in the gaseous outflows of supernova and asymptotic giant branch stars (Daulton et al. 1996); vapor condensation in the evolving solar nebula is also a possibility. These apparently conflicting results reflect one aspect of the uncertainty of the origin of the meteoritic nanodiamonds.

Furthermore, in contrast to the data for trace elements, the isotopic ratios of the major element carbon

and the minor element nitrogen in bulk analyses are similar to solar system ratios (Fig. 1). Swart et al. (1983) and Russell et al. (1996) determined $\delta^{13}C$ ranges from -32 to -38‰ , while $\delta^{15}N$ values were -330‰ for bulk Allende nanodiamonds (Lewis et al. 1983) and $-348 \pm 7\text{‰}$ for bulk nanodiamonds extracted from 11 different primitive chondrites (Russell et al. 1996). δ -values are deviations from standard reference materials in parts per thousand deviations: $\delta^{13}C = [(^{13}C/^{12}C)_{\text{sample}} / (^{13}C/^{12}C)_{\text{PDB}} - 1] \times 10^3$ and $\delta^{15}N = [(^{15}N/^{14}N)_{\text{sample}} / (^{15}N/^{14}N)_{\text{air}} - 1] \times 10^3$, where Vienna-Pee Dee Belemnite and N_2 in air are references for carbon and nitrogen, respectively. Within analytical uncertainty, these $\delta^{15}N$ values are similar to those of the atmosphere of Jupiter ($\delta^{15}N = -374 \pm 82\text{‰}$; Owen et al. 2001) and are close to the values determined for the bulk sun or protosolar nebula and the solar wind ($\delta^{15}N = -383 \pm 8\text{‰}$ and $-407 \pm 7\text{‰}$, respectively; Marty et al. 2011). The nanodiamonds' bulk solar system carbon and nitrogen isotopic compositions, and their absence in certain primitive interplanetary dust particles (Dai et al. 2002) have led to the hypothesis that a fraction of the nanodiamonds could have formed in the early solar system. However, it is important to recognize that the bulk measured $\delta^{13}C$ and $\delta^{15}N$ values from these residues may not be representative of the nanodiamond phase. As noted above, the nanodiamond residues contain a significant component of carbonaceous nondiamond material (Stroud et al. 2011). Furthermore, there may be different populations of meteoritic nanodiamonds with

protosolar nebula and/or presolar origins. Thus, the bulk measured isotopic compositions could be an average over many sources.

Isotopic data from individual presolar grains such as presolar silicon carbide, graphite, silicates, and oxides show large variations, which most likely reflect origins in different stellar sources and via different types of processes (see reviews by Clayton and Nittler 2004; Zinner 2007; Davis 2011). For example, the $^{12}\text{C}/^{13}\text{C}$ ratios of different presolar silicon carbide (SiC) grains span four orders of magnitude (Fig. 1), and the average ratios of the different types of SiC are different from both the terrestrial and solar ratios. Because of the small sizes (average diameter approximately 3 nm; Daulton et al. 1996) of individual diamond grains, isotopic analyses have not been possible due to limitations in spatial resolution and sensitivity, and all isotopic data so far have been obtained from bulk measurements. To shed light on the origin of nanodiamonds, single-grain isotopic analyses are desirable. The distribution of $^{12}\text{C}/^{13}\text{C}$ ratios among meteoritic nanodiamonds can help evaluate whether multiple nanodiamond populations are present in the residues and determine their origin (e.g., solar or presolar). Determining $^{12}\text{C}/^{13}\text{C}$ ratios of individual nanodiamonds also has the potential to distinguish among different presolar stellar sources.

Atom-probe tomography (APT) is currently the only technique with the spatial resolution and detection sensitivity to analyze isotope ratios of individual particles in the size range of meteoritic nanodiamonds (Seidman and Stiller 2009). The objectives of this study are to develop sample preparation techniques that will allow for atom-probe tomographic analyses of individual meteoritic nanodiamonds, to address the questions of their origins as noted above. The idea of using APT to analyze individual meteoritic nanodiamonds was developed independently and contemporaneously in both Chicago and St. Louis. Rather than competing, the two groups decided to collaborate, exchange information, and report their first achievements in a joint publication. In this article, we summarize development of the different sample preparation techniques and analytical protocols, and present our first results of nanodiamond analyses with the atom-probe tomograph at sub-nm spatial resolution. Preliminary results have been presented in conference abstracts (Heck et al. 2010, 2011a, 2011b, 2011c, 2012; Stadermann et al. 2010, 2011; Lewis et al. 2012).

ANALYTICAL METHOD: ATOM-PROBE TOMOGRAPHY

Atom-probe tomography is based on the coupling of a field-ion microscope, a lensless point-projection

instrument that resolves individual atoms on the surface of a sharply pointed (<50 nm) tip at magnifications of greater than 10^6 with sub-nm resolution, with a time-of-flight mass spectrometer (Müller et al. 1968). Atoms on the surface of a specimen at a positive potential with respect to ground are ionized in the presence of a strong electric field (the so-called “field evaporation” effect) and are then repelled from it toward a multichannel plate detector. The pulsed electric field removes surface atoms from a sample on an atom-by-atom and atomic layer-by-layer basis. These field-evaporated ions are detected by a position-sensitive time-of-flight detector on the basis of their mass-to-charge-state ratio (m/q). The detector consists of a microchannel plate with single-ion sensitivity, plus a delay line detector, which sits directly behind it. Because a specimen’s surface is being field-evaporated atomic layer by layer, it is possible to visualize the three-dimensional structure of the sample at an atomic level. In a local-electrode atom-probe (LEAP) tomograph, a cone-shaped local-electrode is placed between a specimen’s microtip and the position-sensitive detector (Fig. 2), effectively confining the electric field to the space between the microtip and the local electrode, which has an orifice diameter of about 30 μm . Samples are introduced into the ultrahigh vacuum analysis chamber and cooled to 20–120 K, before applying a DC voltage to the microtip. The steady DC voltage is maintained just below the threshold of the evaporation field. The threshold for field evaporation is highly dependent on the sample material (i.e., the constituent elements and their bonding) and depends, in particular, on the sublimation and ionization energies and the local work function. To obtain highly controlled pulsed field evaporation and to provide a precise start time for the time-of-flight detector, the microtip is then illuminated with picosecond pulses from a highly focused ultraviolet laser ($\lambda = 355$ nm), resulting in heating of the apex of the microtip, and field ionization and evaporation of the surface atoms. When using a picosecond ultraviolet laser to dissect a microtip, the pulse repetition rate can be up to 1000 kHz. More in-depth descriptions of this technique and its physics can be found in Seidman (2007), Kelly and Miller (2007), Seidman and Stiller (2009), and Kelly and Larson (2012).

For our study, we used two LEAP tomographs developed and manufactured by Cameca Instruments Inc. Most of the analyses were performed with a Cameca LEAP 4000X Si APT with a straight time-of-flight path of 90 mm at the Northwestern University Center for APT (NUCAPT). In one session, we used a Cameca LEAP 4000X HR APT in the Applications Laboratory of Cameca Instruments Inc. This latest-generation instrument (denoted as a LEAP HR

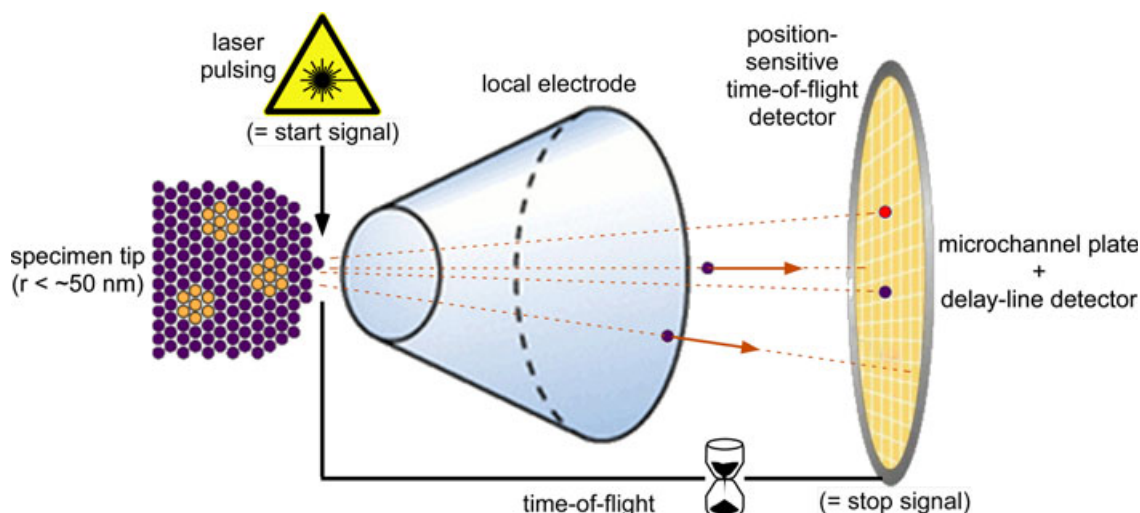


Fig. 2. Schematic of a local-electrode atom-probe tomograph (not to scale). The specimen is maintained at a high positive potential with respect to earth potential, and picosecond laser pulses, impinging on the specimen's microtip approximately perpendicular to the long axis of the microtip, trigger field evaporation of surface atoms. The field-evaporated ions are accelerated along the diverging electric field lines to project a highly magnified image of the microtip's surface onto the position-sensitive time-of-flight detector. The time-of-flight of the ions is used to identify their mass-to-charge-state ratio and hence their chemical identities.

tomograph) is equipped with a reflectron-type time-of-flight mass spectrometer resulting in a flight path of 382 mm and a higher mass resolving power compared with the LEAP 4000X Si (Scheinfein and Seidman 1993).

The LEAP 4000X Si (hereafter simply denoted as a LEAP tomograph) at NUCAPT has received several upgrades over the course of this study and since its original installation in December 2004. The beam conditioning unit and focusing optics received a major upgrade, with the following performance enhancements: (1) the diameter of the laser focus on the microtip was reduced, increasing the energy density of the beam by a factor of four, which permits a shortened heat pulse; (2) a continuous laser pulse energy range spanning 30 fJ–1.5 nJ, equivalent to a 5×10^5 dynamic range, was added, allowing optimum evaporation conditions for a wide variety of materials; (3) the plane of laser polarization can now be rotated in 15° steps from 0 to 90° to vary the precise energy absorption geometry of the laser pulse by the tip; (4) a “ringing” effect that produced spurious peaks in the mass spectrum of some materials was largely eliminated; (5) new motorized in-vacuum optics were added, providing much smoother and better stability with the laser beam alignment; and (6) an active piezoelectric damping system was installed, which efficiently damps all vibrations of the LEAP tomograph. In addition, an upgrade for the LEAP tomograph hardware control PC tripled the maximum data acquisition speed to about 35,000 atoms per second, increasing significantly the throughput of the LEAP tomograph. These enhancements led to significant improvements in data quality over the course of this study.

The laser pulse repetition rate in LEAP tomography has a maximum of 1000 kHz, which makes it possible to measure relatively large volumes of material atom by atom employing reasonable analysis times. The detection efficiency of the microchannel plate detector of the straight-flight path LEAP tomograph ranges from 50 to 60% and is the same for all elements of the periodic table. The efficiency for the LEAP HR tomograph is reduced to 37% due to the field-defining mesh necessary for operation of the reflectron. Its higher signal-to-noise ratio counteracts, however, the sensitivity reduction caused by the lower transmission. Using specialized software (Imago Visualization and Analysis System—IVAS, Cameca Instruments Inc., Kunicki et al. 2006), the data collected can be visualized as three-dimensional distributions of all detected atoms in the analysis volume, at any angle of observation. Time-of-flight mass spectra can be obtained for the entire reconstruction and from selected subvolumes of interest.

SAMPLES

For our study, we selected nanodiamonds from the acid dissolution residue Allende DM, a well-studied nanodiamond isolate (Lewis et al. 1989). The Allende DM isolate consists of a mixture of nanodiamonds and glassy carbon as well as trace minerals (including SiC, graphitic carbon, and metal grains). We used both synthetic detonation nanodiamonds (DNDs) and ultrananocrystalline diamonds (UNCDs) as standards. DNDs are produced in a contained explosion by shock-transformation of organic matter (Greiner et al. 1988).

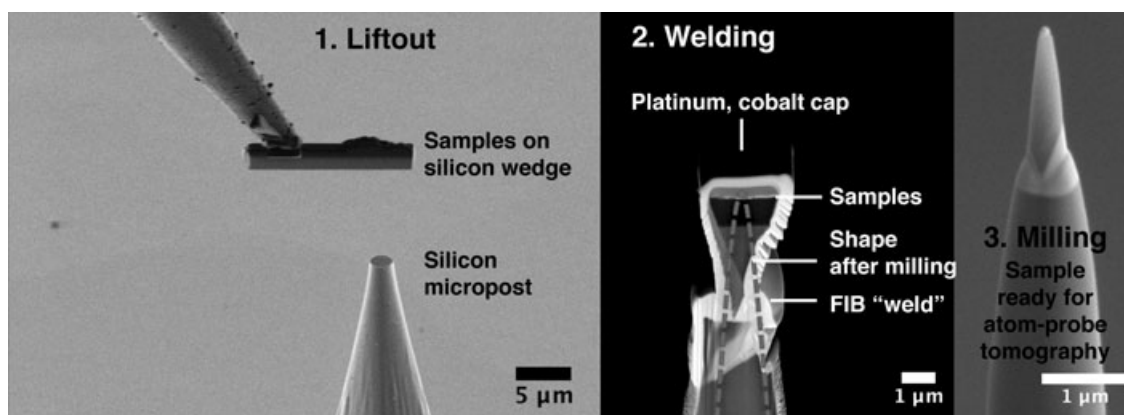


Fig. 3. Focused ion-beam/scanning electron microscopy-based (1) lift-out, (2) “welding,” and (3) milling of a nanodiamond sample deposited on a silicon wafer. After milling, the sample is ready for atom-probe tomography.

and were obtained from Lawrence Livermore National Laboratory. UNCD films are grown by microwave-plasma deposition at Argonne National Laboratory (Auciello and Sumant 2010) directly onto silicon microtips.

SAMPLE PREPARATION METHODS

To be suitable for APT analyses, samples must be shaped into a sharp microtip with an apex radius of about 50 nm and must be able to withstand the high mechanical stresses present during the analyses. We used several procedures to prepare samples that satisfy these requirements. Material imperfections and weakly bonded interfaces can lead to catastrophic microtip failure and arcing. In the following, we describe briefly the methods developed independently by the Chicago and St. Louis groups.

Chicago Methods

For preparation of the atom-probe tomographic samples of meteoritic or synthetic DNDs, the grains were suspended in an ultrasonicated mixture of isopropanol (Fisher Optima) and water (Millipore Milli-Q). A 2–4 μL drop of the suspension was deposited onto a clean silicon substrate and evaporated with a heat lamp. To fill open pore space and stabilize the samples, atomic layer deposition (ALD; Elam et al. 2006) was performed at Argonne National Laboratory to deposit Al_2O_3 (approximately 3.6 nm thickness) and tungsten (approximately 1.3 nm thickness) onto the tips. We also prepared control samples that consisted only of deposited Al_2O_3 .

Method 1: In our first approach, the nanodiamond suspension was deposited on a flat silicon wafer. After ALD, the wafer was coated with 60–500 nm of sputter-

deposited cobalt to protect the nanodiamonds from the Ga^+ focused ion-beam (FIB) during subsequent milling in the FIB microscope. A wedge-shaped prism was milled with dual-beam FIB microscopes at Argonne National Laboratory (Zeiss 1540XB and Zeiss NVision) or at Northwestern University (FEI Helios), lifted out, and welded onto a flat-top silicon micropost (Thompson et al. 2005) with carbon and platinum (Fig. 3). To enhance stability, carbon- and platinum-cold-welds were applied on at least two sides. Subsequently, the welded wedge was FIB-milled (Ga^+ ions) with an annular mask into a sharp microtip (Larson et al. 1999). The cobalt cap-layer served as a marker and Ga^+ ion-beam milling was stopped before the last bit of cobalt disappeared.

Method 2: In this approach, a drop of the same suspension was placed onto an array of presharpended silicon microtips (Cameca) to cover the whole microtip array, which was then suspended upside down and exposed to a heat lamp for evaporation. Following that, ALD was performed; no additional sample preparation was required for this method. This method has the advantage that there is no possible Ga^+ ion-beam damage to the diamonds from the dual-beam FIB microscope.

As the final step before analysis, microtips prepared by both methods were imaged by scanning electron microscopy to verify that they were sufficiently sharp for field evaporation in the atom probe. To minimize oxidation, the samples were loaded into the ultrahigh vacuum chamber of the APT within a few hours to a day after sample preparation.

St. Louis Method

Meteoritic (or synthetic) nanodiamonds were suspended in a mixture of alcohol and water for

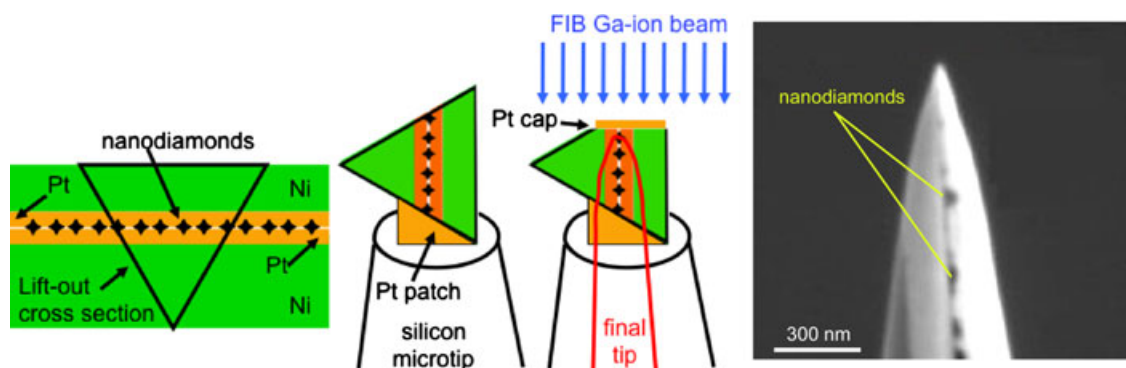


Fig. 4. Left: schematic illustrating the focused ion-beam (FIB)-microscope extraction and rotation of a nanodiamond sandwich for ion milling and atom-probe tomography analysis. Right: secondary electron image of a nanodiamond sandwich microtip showing Allende nanodiamonds embedded in a platinum matrix.

deposition onto a high-purity nickel substrate. A thin (170 nm) layer of platinum was deposited onto the nickel substrate by ion-beam sputter deposition, followed by deposition of the nanodiamonds from the suspension onto the platinum-covered nickel substrate (Isheim et al. 2013). To prevent the nanodiamonds from clustering, the suspension was ultrasonicated until immediately before deposition. The sample was also ultrasonicated during evaporation of the suspension drop to prevent nanodiamonds from agglomerating along the rim of the drop during drying and to obtain more uniform deposition layers on the substrate. To protect the nanodiamonds from surface contamination and to provide a solid-host material for the grains, the sample was then coated with an additional layer of platinum, followed by a final 500 nm layer of nickel to serve as a cover during subsequent FIB milling, thereby creating a Ni-Pt-diamond-Pt-Ni sandwich structure. Sections of this deposition layer were lifted out utilizing the FEI Helios dual-beam FIB microscope at Northwestern University or the FEI Quanta dual-beam FIB at Washington University in St. Louis. Approximately 3 μm long sections of these lift-outs were attached to prefabricated silicon microposts and milled into sharp microtips with a Ga^+ ion-beam. This method resulted in microtips that contained nanodiamonds in a horizontal layer in close proximity to the pointed end of the column. These early microtips often suffered from mechanical failures along the horizontal nanodiamond layer and led us to modify the sample preparation procedure by rotating the FIB-microscope-extracted section, so that the nanodiamond layer is parallel (cross section mode; Lawrence et al. 2008), rather than perpendicular, to the long axis of the microtip (Fig. 4). This improves the mechanical stability of the microtip and allows sequential field evaporation of individual or small clusters of nanodiamonds over a larger deposition layer.

DATA PROCESSING

Cameca's data processing software, IVAS, was used to create tomographic reconstructions. IVAS can produce and export mass spectra from the integrated data set of an entire microtip or of selected regions of interest (ROIs) within a tip. In IVAS, ROIs can be defined in several different ways: (1) by using a gridded isoconcentration surface calculation that applies a threshold function to envelop volumes of defined density ranges or elemental concentration ranges; (2) by using a cluster algorithm (Marquis and Hyde 2010); and (3) by manually defining a geometric shape (e.g., spheroid) and centering it on a concentration hotspot. We used both the manual method and the threshold isoconcentration surface function to define ROIs for most of the samples.

Uncertainties on Carbon Isotope Peak Ratios

Spectral data of integrated microtips and ROIs were exported from IVAS to integrate the area under peaks, calculate peak ratios, and to create mass spectra. Uncertainties in the peak ratios of isotopes can result from the background correction, hydride interferences, and potential instrumental biases.

A background correction is not necessary if the signal-to-noise ratio is high, but can constitute a major uncertainty if the peak intensities are only slightly above background. Background corrections were made in two ways: (1) automatic background correction by IVAS consists of the subtraction of a fitted function that describes the time-independent background throughout the time-of-flight mass spectrum; and (2) a manual background correction can be made by subtraction of the integrated linear interpolation of the background baseline from the integrated peak. The data from the Chicago group were background-corrected using the

Table 1. Carbon isotope peak ratios for integrated microtips from the Chicago group.

| Sample | $^{12}\text{C}^+ / ^{12}\text{C}^{++}$ | $^{12}\text{C}^+ / ^{13}\text{C}^+$ | $^{12}\text{C}^{++} / ^{13}\text{C}^{++}$ | T (K) | E (pJ) | Comments |
|-------------------------------|--|-------------------------------------|---|---------|----------|---|
| <i>Synthetic Nanodiamonds</i> | | | | | | |
| DND 15874 L11 PSM04 | 2.3 ± 0.6 | 41 ± 26 | 45 ± 45 | 80 | 300 | |
| UNCD 113207 PSM03 | 6.1 ± 0.9 | 77 ± 12 | (198 ± 120) | 80 | 200 | Low $^{13}\text{C}^{++}$ counts make $^{12}\text{C}^{++} / ^{13}\text{C}^{++}$ peak ratio doubtful. Upgraded laser optics: smaller spot size. |
| UNCD 113215 PSM04 | 1.6 ± 0.1 | 10 ± 1 | 63 ± 19 | 80 | 50 | Upgraded laser optics: smaller spot size. |
| UNCD 113225 PSM08 | 2.8 ± 0.2 | 40 ± 4 | 67 ± 16 | 80 | 100 | |
| UNCD 113233 PSM10 | 2.7 ± 0.3 | 89 ± 14 | 68 ± 24 | 80 | 150 | |
| Mean | 2.3 ± 0.2 | 36 ± 3 | 65 ± 11 | | | |
| <i>Allende Nanodiamonds</i> | | | | | | |
| ADM 14973 L08 M14 | 4.6 ± 0.4 | 49 ± 4 | 39 ± 7 | 110 | 300 | Sandwich method |
| ADM 15122 L08 M01 | 4.2 ± 0.3 | 32 ± 3 | 87 ± 47 | 110 | 300 | |
| ADM 15961 L09 M29 | 12 ± 1 | 71 ± 7 | (28 ± 6) | | | Low $^{13}\text{C}^{++}$ counts make $^{12}\text{C}^{++} / ^{13}\text{C}^{++}$ peak ratio doubtful. |
| ADM 15963 L09 M17 | 9.5 ± 0.6 | 36 ± 2 | 51 ± 15 | 110 | 300 | |
| ADM 15964 L09 M16 | 12 ± 1 | 31 ± 3 | (6 ± 1) | 110 | 300 | Low $^{13}\text{C}^{++}$ counts make $^{12}\text{C}^{++} / ^{13}\text{C}^{++}$ peak ratio doubtful. |
| ADM 15971 L09 M30 | | 78 ± 9 | | 110 | 300 | No significant C^{++} counts. |
| ADM 17134 L17 PSM25 | (5.0 ± 0.4) | (3.9 ± 0.3) | 41 ± 97 | 80 | 20 | Upgraded laser optics: smaller spot size. Large peak at mass-to-charge-state ratio of 13, possibly large hydride interference makes $^{12}\text{C}^+ / ^{13}\text{C}^+$ ratio doubtful. |
| ADM 17137 L17 PSM15 | 3.2 ± 0.6 | 20 ± 3 | 17 ± 10 | 80 | 20 | Upgraded laser optics: smaller spot size. |
| Mean | 7.9 ± 0.2 | 43 ± 1 | 47 ± 10 | | | |

Errors are 2σ and are based on counting statistics. Means are ratios of integrated counts for each ion species and do not include unreliable data, which are given in parentheses and italics. The nominal set temperatures (T) of the microtips and the nominal laser pulse energies (E) are also given. A LEAP 4000X HR was used for UNCDs; a LEAP 4000X Si was used for all other samples.

first method, whereas data from the St. Louis group were corrected using the second method. Comparison on several spectra indicates that both methods produce similar results.

Another uncertainty is the potential contribution of the $(^{12}\text{C}^1\text{H})^+$ hydride interference to the $^{13}\text{C}^+$ peak (separated by approximately 0.0045 U). Neither of the LEAP tomograph systems used has a mass resolving power sufficient to resolve this interference. Previous ion-probe microanalyses have detected a high concentration of hydrogen in nanodiamond isolates (Virag et al. 1989), and Fourier-transform infrared spectroscopy has shown the presence of carboxyl ($-\text{COOH}$) surface groups (Lewis et al. 1989) in Allende DM isolates. As half of the carbon atoms in an average-sized meteoritic nanodiamond are within one unit cell of the surface, surface-absorbed species are an important source of hydrogen. In addition, hydride formation can result from the presence of residual hydrogen in the LEAP tomograph. The partial pressure of hydrogen in the analysis chamber is measured with a residual gas analyzer and can be highly variable. Therefore, a constant correction factor cannot be used, and, in fact, to the best of our knowledge, no

correction method for hydride formation during field evaporation based on hydrogen partial pressure is known. The probability of forming doubly charged hydrides is expected to be much lower than for singly charged hydrides, so we do not anticipate significant hydride interferences for $^{13}\text{C}^{++}$. We therefore optimized the analytical conditions to decrease the $\text{C}^+ / \text{C}^{++}$ charge-state-ratio and increase the signal at $^{13}\text{C}^{++}$. This is done by decreasing the temperature at which field evaporation occurs (decreasing the laser pulse energy), which results in the requirement of a higher voltage for field evaporation (Kingham 1982). The charge-state-ratio cannot, however, be decreased indefinitely; higher voltages and lower laser pulse energy decrease sample stability due to the higher mechanical Maxwell stresses induced at higher electric fields, which result in more frequent tip fractures. In this study, we were able to achieve minimum $\text{C}^+ / \text{C}^{++}$ ratios of approximately 2–3 (Tables 1 and 2). For better readability throughout the manuscript, we label peaks with only the major ion species thought to be responsible for the peak in the mass spectrum, although there can be contributions from isobarically interfering hydrides or other species.

Table 2. Carbon isotope peak ratios for integrated microtips from the St. Louis group.

| Sample | $^{12}\text{C}^+ / ^{12}\text{C}^{++}$ | $^{12}\text{C}^+ / ^{13}\text{C}^+$ | $^{12}\text{C}^{++} / ^{13}\text{C}^{++}$ | $T(\text{K})$ | $E(\text{pJ})$ | Comments |
|-------------------------------|--|-------------------------------------|---|---------------|----------------|---|
| <i>Synthetic Nanodiamonds</i> | | | | | | |
| DND R06 17619 A61 M35 | 2.2 ± 1.1 | 38 ± 16 | | 80 | 40 | No significant C^{++} counts. Upgraded laser optics: smaller spot size. |
| DND R06 17620 A61 M35 | 1.9 ± 0.5 | 60 ± 10 | 61 ± 16 | 80 | 40 | Upgraded laser optics: smaller spot size. |
| DND R06 17621 A61 M34 | 15.2 ± 2.5 | 31 ± 10 | | 80 | 40 | No significant C^{++} counts. Upgraded laser optics: smaller spot size. |
| DND R06 17626 A62 M4 | 3.1 ± 0.4 | 76 ± 12 | 64 ± 20 | 55 | 80–100 | Upgraded laser optics: smaller spot size. |
| DND R06 17629 A61 M31 | 10.7 ± 1.2 | 10 ± 2 | | 55 | 70–90 | No significant C^{++} counts. Upgraded laser optics: smaller spot size. |
| DND R06 16013 A46 M1 | 3.8 ± 0.5 | 57 ± 22 | | 103 | 150 | No significant C^{++} counts. |
| DND R06 17967 A62 M35 | 1.5 ± 0.2 | 30 ± 14 | <i>(122 ± 306)</i> | 54 | 40 | Low $^{13}\text{C}^{++}$ counts make $^{12}\text{C}^{++} / ^{13}\text{C}^{++}$ peak ratio doubtful. Upgraded laser optics: smaller spot size. |
| DND R06 17969 A62 M28 | 1.8 ± 0.1 | 53 ± 10 | 57 ± 16 | 54 | 40 | Upgraded laser optics: smaller spot size. |
| DND R06 17978 A62 M34 | 4.2 ± 1.3 | 30 ± 12 | | 95 | 40 | No significant C^{++} counts. Upgraded laser optics: smaller spot size. |
| DND R06 18428 A64aM34 | 2.2 ± 0.4 | 72 ± 24 | 71 ± 44 | 95 | 40–80 | Upgraded laser optics: smaller spot size. |
| Mean | 3.0 ± 0.1 | 46 ± 2 | 64 ± 7 | | | |
| <i>Allende Nanodiamonds</i> | | | | | | |
| ADM R06 15004 A36 M1 | 1.6 ± 0.4 | 61 ± 18 | 54 ± 20 | 95 | 150 | |
| ADM R06 15005 A36 M1 | 1.1 ± 0.2 | 45 ± 16 | 83 ± 48 | 95 | 150 | |
| ADM R06 16096 A47 M10 | 1.7 ± 0.4 | 96 ± 30 | 72 ± 26 | 103 | 150 | |
| ADM R06 16097 A47 M11 | 1.7 ± 0.6 | 87 ± 42 | 87 ± 58 | 102 | 150 | |
| ADM R06 16098 A47 M12 | 1.9 ± 0.5 | 74 ± 28 | 73 ± 44 | 103 | 150 | |
| ADM R06 16119 A47 M12 | 2.2 ± 0.6 | 69 ± 28 | <i>(189 ± 350)</i> | 103 | 150 | Low $^{13}\text{C}^{++}$ counts make $^{12}\text{C}^{++} / ^{13}\text{C}^{++}$ peak ratio doubtful. |
| ADM R06 16120 A47 M13 | 1.8 ± 0.4 | 77 ± 16 | 87 ± 30 | 102 | 250 | |
| ADM R06 18430v01 A65a M06 | 2.0 ± 0.3 | 36 ± 6 | 105 ± 70 | 95 | 40–100 | Upgraded laser optics: smaller spot size. |
| ADM R06 18436v01 A65a M05 | 1.8 ± 0.6 | 92 ± 44 | 72 ± 40 | 95 | 40 | Upgraded laser optics: smaller spot size. |
| ADM R06 18437 A65a M04 | 1.8 ± 0.4 | 57 ± 8 | 47 ± 10 | 95 | 40–80 | Upgraded laser optics: smaller spot size. |
| Mean | 2.0 ± 0.1 | 69 ± 4 | 65 ± 5 | | | |

Errors are 2σ and are based on counting statistics. Means are ratios of integrated counts for each ion species and do not include unreliable data, which are given in parentheses and italics. The nominal set temperatures (T) of the microtips and the nominal laser pulse energies (E) are also given.

RESULTS AND DISCUSSION

Mass Spectra and Tomographic Reconstructions

We define a successful APT measurement as one that results in the detection of major peaks of ^{12}C and

^{13}C with a high signal-to-noise ratio in the mass spectrum and the visualization of carbon-rich regions in the 3-D tomographic reconstructions of a microtip. While some of our microtips failed, all sample preparation methods produced specimens that were successfully analyzed. Representative mass spectra of

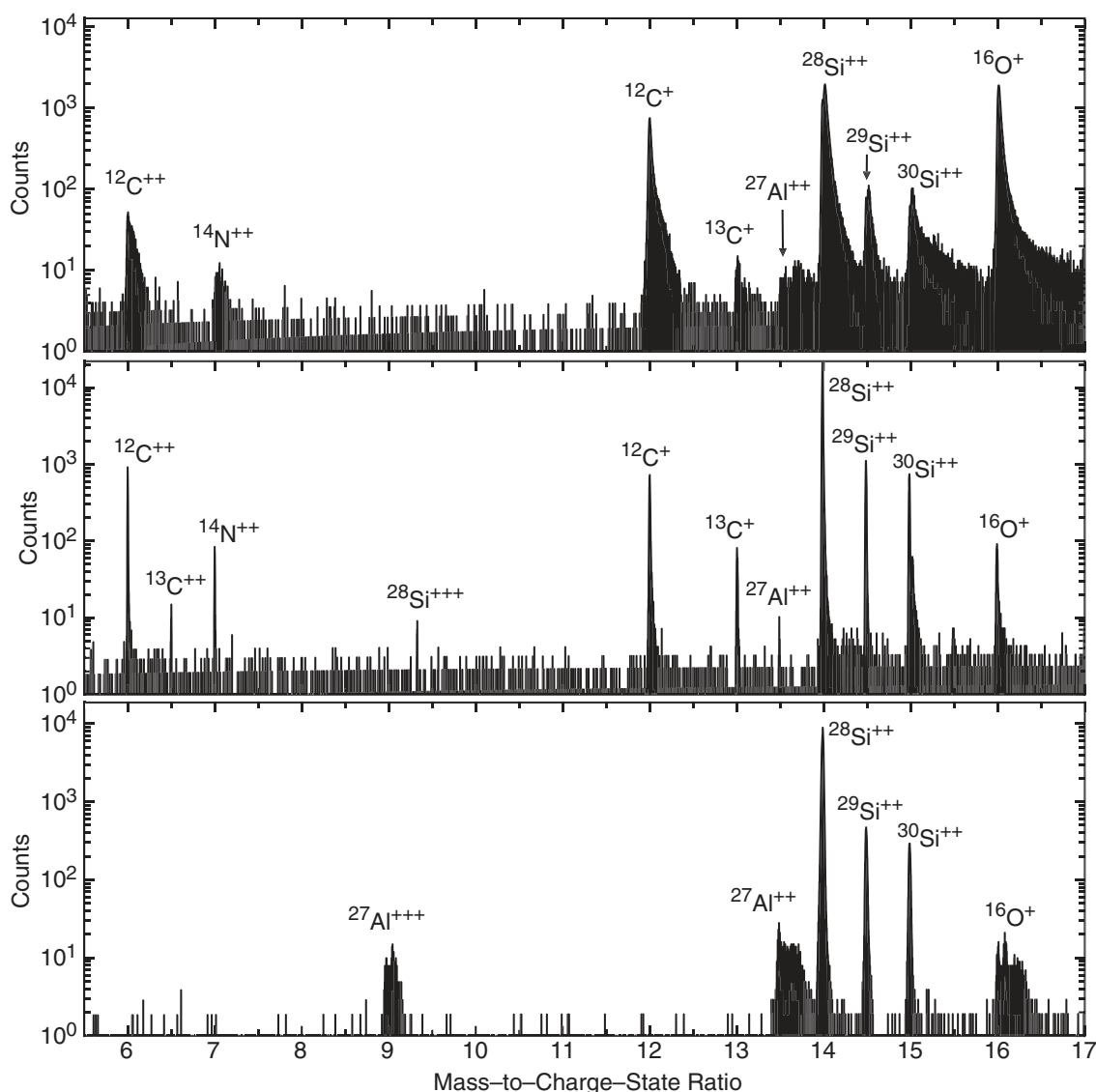


Fig. 5. Representative mass spectra; the mass-to-charge-state ratio range was selected to display carbon isotope peaks. Top: Meteoritic nanodiamonds (direct deposition method) analyzed with the local-electrode atom-probe (LEAP) 4000X Si before the ultraviolet laser optics upgrade. Middle: Synthetic nanodiamonds (UNCD) analyzed with the upgraded LEAP 4000X HR using a 355 nm wavelength laser. Bottom: No significant carbon peaks are visible in the “blank” measurement of a silicon microtip atomic layer deposition-coated with alumina analyzed with the upgraded LEAP 4000X Si. Note the narrower peaks in the middle and bottom spectra that are the result of heating a smaller volume due to the smaller spot size obtained using a 355 nm laser.

meteoritic and synthetic nanodiamonds and of a blank are displayed in Fig. 5. As a result of progressive instrument upgrades and improved sample preparation techniques, data quality increased over the 3 years of this study and resulted, in general, in narrower peaks, lower background noise (i.e., improved signal-to-noise ratios), and longer runs due to improved sample stability.

The tomographic 3-D reconstructions show different sample geometries resulting from the different preparation techniques utilized (Figs. 6 and 7). Figure 6

shows 3-D reconstructions from the ALD and direct deposition methods used by the Chicago group. A densely packed nanodiamond layer is useful to obtain integrated data for a large number of nanodiamonds, comparable to a bulk analysis (Fig. 6, left), whereas the direct deposition method results in nanodiamonds that coat the surface of the silicon microtip with a much higher dispersion (Fig. 6, right). The degree of dispersion depends on the colloidal diamond concentration at the time of deposition. Direct deposition is, therefore, the preferred method to obtain

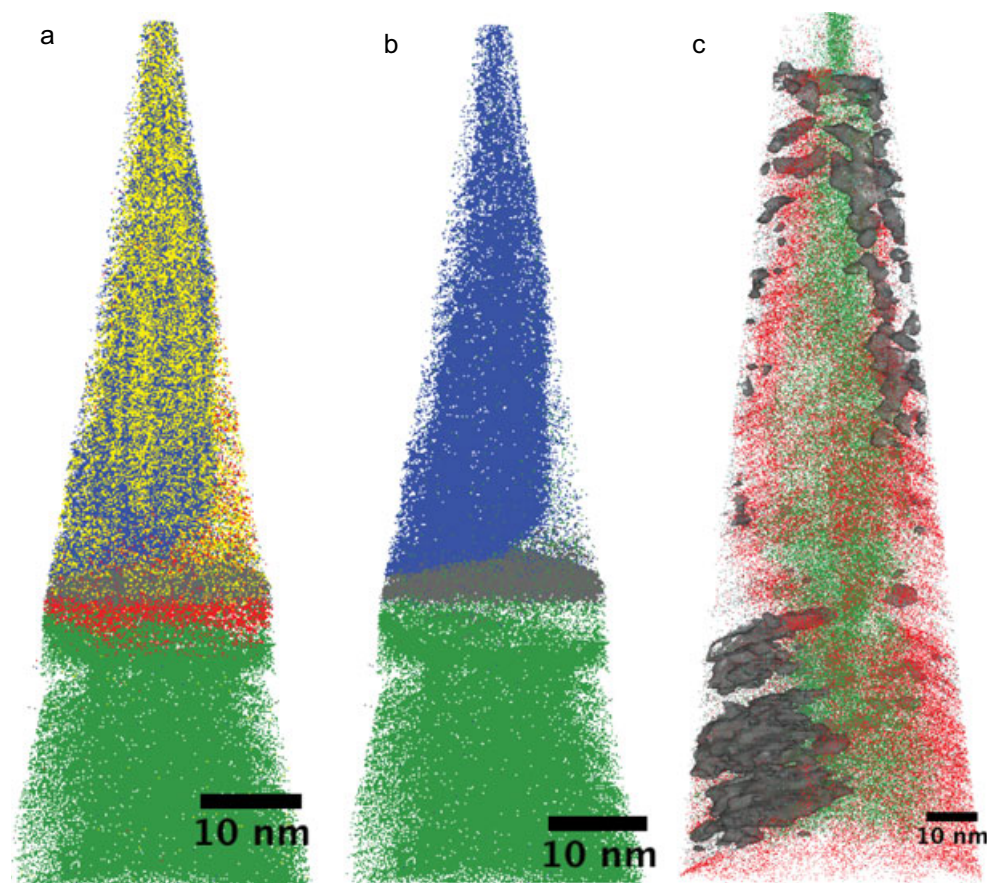


Fig. 6. 3D-tomographic atom-probe tomography reconstructions of nanodiamonds: Each dot represents a single detected atom. Atoms are color coded (carbon gray, oxygen red, cobalt blue, silicon green, gallium yellow). a) Allende DM sample sandwiched between a flat-top silicon microtip and a cobalt cap. b) Same as left but without gallium and oxygen atoms to better display carbon. c) Allende DM sample coating a presharpener silicon microtip. Carbon isoconcentration surfaces are shaded gray and exhibit carbon-rich regions representing nanodiamonds, clusters of nanodiamonds, and associated disordered carbon on the surface of the microtip. The aspect ratio and scale are approximate in all reconstructions.

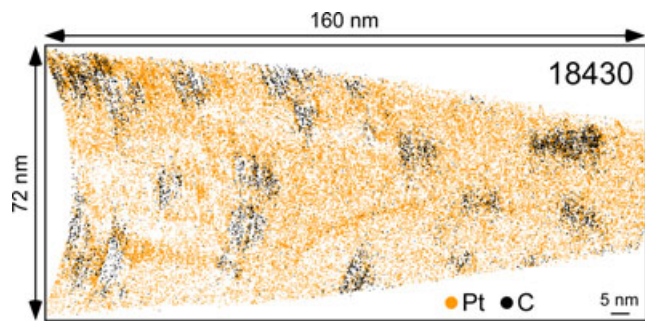


Fig. 7. 3D-tomographic reconstruction of meteoritic nanodiamonds from the Allende DM residue embedded in a platinum matrix. Each dot represents a single atom of platinum (orange) or carbon (black). Note that for clarity, only a fraction of the total platinum atoms are displayed (other atoms present within the analysis are also not shown).

data from individual nanodiamonds. Figure 7 shows the reconstruction of a meteoritic nanodiamond analysis using the Ni-Pt-diamond-Pt-Ni sandwich method of the

St. Louis group. Rotation of the FIB microscope lift-out, such that the nanodiamond layer is parallel to the long axis of the microtip, results in dispersion of the nanodiamonds and, like the Chicago direct deposition method, permits the analysis of individual or small clusters of nanodiamonds.

Carbon Isotope Peak Ratios

Carbon isotope peak ratios, based on the background-corrected counts of ^{12}C and ^{13}C integrated over entire microtips, of meteoritic and synthetic nanodiamonds are displayed in Fig. 8 and are listed in Tables 1 and 2 for the Chicago and St. Louis groups, respectively. It is important to note that it is not possible to distinguish between nanodiamonds and disordered carbon phases in our 3-D tomographic reconstructions, and therefore, our results represent averages of those two phases. In both data sets,

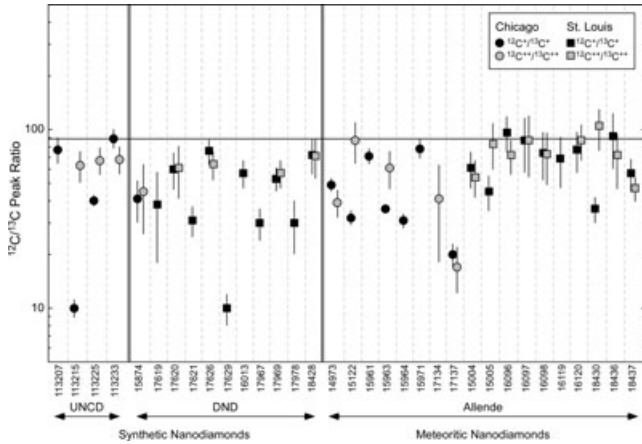


Fig. 8. Carbon isotope peak ratios of synthetic (DND and UNCD) and meteoritic Allende nanodiamonds measured by atom-probe tomography. Data are the integrated carbon ions detected in entire microtips. Run numbers correspond to those listed in Tables 1 and 2. The horizontal line corresponds to the terrestrial $^{12}\text{C}/^{13}\text{C}$ ratio of 89 (Coplen et al. 2002). Error bars are 2σ and are based on counting statistics. Large error bars reflect low total ion counts for $^{13}\text{C}^+$ and especially $^{13}\text{C}^{++}$.

$^{12}\text{C}^{++}/^{13}\text{C}^{++}$ ratios could not be determined for some microtips, due to the small number of $^{13}\text{C}^{++}$ counts, and only $^{12}\text{C}^+/^{13}\text{C}^+$ ratios are reported. In most cases where statistically significant ratios could be reported for both doubly and singly charged carbon, the two ratios are in fairly good agreement. In six data sets, where the two ratios do not agree, however, the singly charged ion ratio is lower than the doubly charged ion ratio. This difference can be understood in terms of the $^{12}\text{C}^1\text{H}^+$ hydride contribution to $^{13}\text{C}^+$ noted above, which will lead to lower ratios. This is shown more clearly in a plot of $^{12}\text{C}^+/^{13}\text{C}^+$ versus $^{12}\text{C}^{++}/^{13}\text{C}^{++}$ peak ratios (Fig. 9), where most of the data lie on a 45° line showing agreement between ratios of singly and doubly charged ions. The data points that plot below the correlation line have lower $^{12}\text{C}^+/^{13}\text{C}^+$ ratios than $^{12}\text{C}^{++}/^{13}\text{C}^{++}$ ratios, an indication that the $^{13}\text{C}^+$ peaks contain a contribution from hydride ($^{12}\text{C}^1\text{H}^+$). The lack of data points significantly to the left of the line indicates that hydride (or other) contributions to the $^{13}\text{C}^{++}$ peaks are insignificant compared with those at $^{13}\text{C}^+$.

Comparing the data for all synthetic and meteoritic nanodiamonds (Tables 1 and 2) shows that almost all ratios are lower than the terrestrial $^{12}\text{C}/^{13}\text{C}$ ratio of 89 (Figs. 8 and 9). While the meteoritic nanodiamonds could, in principle, exhibit large natural deviations from the terrestrial value, the same is not true of the synthetic nanodiamonds. This indicates that, in addition to the statistical uncertainties, there is a currently

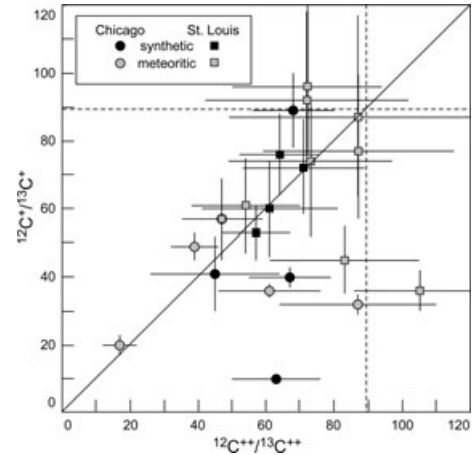


Fig. 9. Plot of $^{12}\text{C}^{++}/^{13}\text{C}^{++}$ versus $^{12}\text{C}^+/^{13}\text{C}^+$ peak ratios for meteoritic and synthetic tips from the Chicago and St. Louis data sets. The dashed lines correspond to the terrestrial $^{12}\text{C}/^{13}\text{C}$ ratio of 89 (Coplen et al. 2002). The diagonal line indicates agreement between ratios for singly and doubly charged ions.

unidentified uncertainty present, an instrumental bias, which is responsible for the deviation of the measured isotope peak ratios from the expected value. One possible source for this uncertainty may be variations in sample type and, particularly, in analytical conditions. As noted earlier, the LEAP instrument underwent significant upgrades throughout the 3 yr period of study, potentially affecting the reproducibility of results. More important may be that both the Chicago and the St. Louis groups experimented with varying analytical parameters during the measurements, particularly in the early stages of this study, to determine the optimum conditions for field evaporation of these complex samples. Future work on nanodiamond samples, prepared in the same way and analyzed under similar conditions, should minimize such variations.

Instrumental bias can also occur in the case of a multiple event, when multiple ions impact the detector during the same pulse cycle. If these ions impact close enough together in time or location, deadtime or deadspace events can occur due to the (3 ns) signal resolution time. The pile-up effect occurs if enough ions trigger pulses on the delay-lines before the signals from the first ion are processed (Gault et al. 2012). At higher evaporation rates, these effects increase as the probability of multiple events increases and will result in an underestimation of the affected ion species. During our analyses, we usually experienced low evaporation rates. When encountering interfaces between materials with different field evaporation thresholds, however, bursts of ions can be generated simultaneously from a small volume and result in uncounted impacts (De

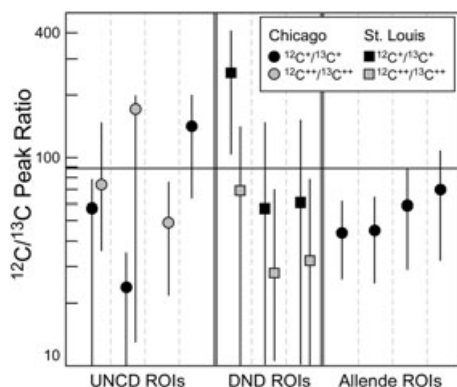


Fig. 10. Carbon isotope peak ratios of regions of interest defined from selected synthetic (DND and UNCD) and meteoritic Allende nanodiamond tips. The horizontal line corresponds to the terrestrial $^{12}\text{C}/^{13}\text{C}$ ratio of 89 (Coplen et al. 2002). Error bars are 2σ and are based on counting statistics.

Geuser et al. 2007). Moreover, it is well known that carbon is an element that is prone to evaporation as multiple events (Andr n et al. 1980). This effect would result in preferential undercounting of the dominant isotope (^{12}C in this case), leading to $^{12}\text{C}/^{13}\text{C}$ ratios that are systematically too low, as observed in most of our data sets (Figs. 8 and 9).

For selected meteoritic and synthetic nanodiamond tips, we were able to determine carbon isotope peak ratios for carbon-rich ROIs with sizes similar to those of individual nanodiamonds (Fig. 10). Determination of the appropriate size for the region of interest is not entirely straightforward. In APT, the evaporation field for carbon is significantly higher than that of any viable substrate material (Southworth and Ralph 1969; Tsong 1978). Because of this difference, the nanodiamond

inclusions will resist field evaporation until the surrounding matrix has been removed, exposing a smaller radius nub on the larger tip, leading to a local magnification effect (e.g., Miller and Hetherington 1991) of the carbon inclusions in the x - and y -directions. We therefore selected ROIs centered on the carbon-rich areas that were larger in the x - and y -directions to account for this effect. An individual nanodiamond contains approximately 2000 atoms; with a 50% detection efficiency, we expect to be able to count approximately 1000 of these. The ROIs defined here contain approximately 800–1000 atoms, substantiating this approach to taking the local magnification effect into account. The carbon isotope peak ratios determined from these ROIs have values consistent with those of the larger microtips from which they originate. Within the admittedly rather large uncertainties, we do not see any significant differences between the ratios from the meteoritic and synthetic nanodiamonds (Fig. 10).

Silicon Isotope Peak Ratios

Finally, we also obtained silicon isotope peak ratios from the silicon microtips used in the Chicago group experiments, as the silicon surface is exposed after the nanodiamond-bearing cover has evaporated. As for carbon in the synthetic nanodiamond samples, we expect the Si isotope ratios for both singly and doubly charged ions to be consistent with the terrestrial values. Figure 11 shows, however, that both $^{29}\text{Si}/^{28}\text{Si}$ and $^{30}\text{Si}/^{28}\text{Si}$ ratios show deviations from normal. The shift toward higher $^{29}\text{Si}^+/^{28}\text{Si}^+$ ratios compared with $^{29}\text{Si}^{++}/^{28}\text{Si}^{++}$ (Fig. 11, left panel) can be best explained by an isobaric interference of $(^{28}\text{Si}^1\text{H})^+$ on

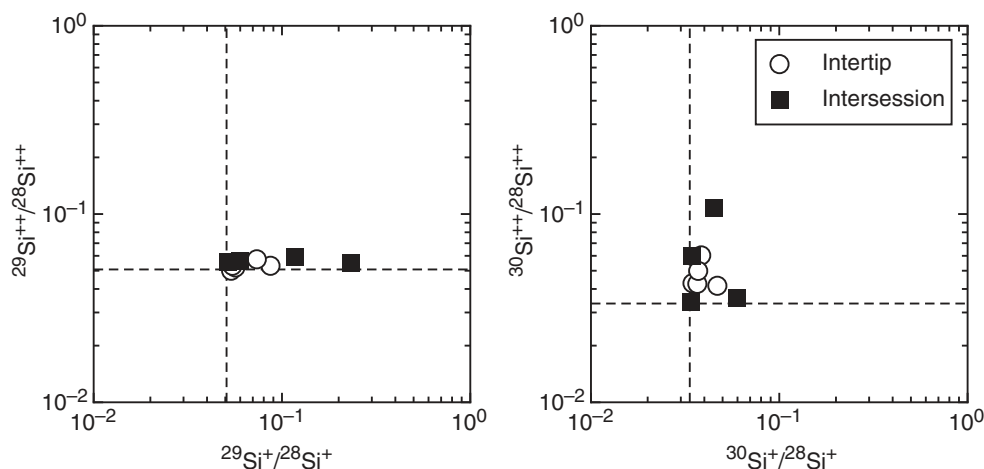


Fig. 11. Background-corrected silicon isotope peak ratios from silicon microtips analyzed with the LEAP tomography within the same session (intertip) and in different sessions (intersession). 2σ error bars are based on counting statistics and are smaller than the symbol sizes. The dashed lines represent terrestrial (normal) isotope ratios from Coplen et al. (2002).

$^{29}\text{Si}^+$. The considerable variability in the $^{29}\text{Si}^+ / ^{28}\text{Si}^+$ ratios probably reflects variability in hydride formation. Isobaric interferences due to hydrides should affect ^{29}Si more than ^{30}Si , because ^{29}Si has a much lower abundance than ^{28}Si . The higher $^{30}\text{Si}^{++} / ^{28}\text{Si}^{++}$ ratios compared with $^{30}\text{Si}^+ / ^{28}\text{Si}^+$ ratios (Fig. 11, right panel) are more difficult to understand, but may be due to a variable isobaric interference of CH_3^+ with $^{30}\text{Si}^{++}$, inflating the $^{30}\text{Si}^{++}$ peak.

CONCLUSIONS AND OUTLOOK

We have developed sample preparation methods and optimized analytical conditions for stable APT analyses of nanodiamonds, such that carbon isotopic peak ratios can be determined on a routine basis. Additional work is, however, required to understand completely the analytical biases affecting these measurements. We are currently preparing nanodiamond standards with different isotopic compositions, which will allow us to compare the ion-peak ratios with the expected isotope ratios for different compositions. In addition to allowing us to confirm (or not) a linear relationship between the measured and true ratios, analyzing standards with different isotopic compositions can provide information on the relative importance of various artifacts or biases present in our data. For example, the analysis of a nanodiamond standard consisting only of ^{12}C can provide constraints on the importance of the hydride contribution at mass 13. Understanding the variations that we observe in our data sets for synthetic nanodiamond samples is an important prerequisite to understanding and interpreting data for meteoritic nanodiamonds.

Two additional intrinsic problems with analyzing individual nanodiamonds are as follows: (1) the limited number of atoms available, leading to relatively large uncertainties; and (2) the presence of a second carbon allotrope (disordered carbon) in the diamond-bearing residues. Despite these challenges, we anticipate that APT will prove to be a powerful technique for analyzing the elemental and isotopic compositions of extraterrestrial nanoparticles, and that useful cosmochemical data for meteoritic nanodiamonds can be obtained.

Acknowledgments—We thank R. S. Lewis for providing the Allende nanodiamond sample, K. Knight for the detonation diamonds, J. Pearson for sputter coating, and D. Schreiber for helpful discussions. We are grateful to I. Lyon, L. Nittler, and J. Matsuda for careful and constructive reviews, which significantly improved this article. This study is supported by NASA grants NNX09AC28G and NNX13AF53G (C.F.),

NNX09AG39G (A.M.D. and T.S.), NNX11AG77G (P.R.H.), and by the Tawani Foundation. Atomic layer deposition, UNCD film growth, and some of the FIB microscope work were performed at Argonne National Laboratory. Assistance with UNCD film growth and APT analysis was supported by the US Department of Energy, Office of Science Materials Sciences and Engineering Division, under Contract No. DE-AC02-06CH11357 (M.R.S., M.J.P., O.A.). The NUCAPT LEAP was purchased and upgraded with funding from NSF-MRI (DMR-0420532) and ONR-DURIP (N00014-0400798, N00014-0610539, N00014-0910781) grants. This study was also supported by the National Science Foundation's MRSEC program (DMR-1121262) and made use of its Shared Facilities at the Materials Research Center of Northwestern University. We also gratefully acknowledge the Initiative for Sustainability and Energy at Northwestern (ISEN) for grants to upgrade the capabilities of NUCAPT.

Editorial Handling—Dr. Ian Lyon

REFERENCES

- Andr n H. O., Henjered A., and Nord n H. 1980. Composition of MC precipitates in a titanium stabilized austenitic stainless steel. *Journal of Materials Science* 15:2365–2368.
- Atreya S. K., Mahaffy P. R., Niemann H. B., Wong M. H., and Owen T. C. 2003. Composition and origin of the atmosphere of Jupiter—An update, and implications for the extrasolar giant planets. *Planetary and Space Science* 51:105–112.
- Auciello O. and Sumant A. V. 2010. Status review of the science and technology of ultrananocrystalline diamond (UNCDTM) films and application to multifunctional devices. *Diamond and Related Materials* 19:699–718.
- Clayton D. D. and Nittler L. R. 2004. Astrophysics with presolar stardust. *Annual Review of Astronomy and Astrophysics* 42:39–78.
- Coplen T. B., B hlke J. K., De Bi vre P., Ding T., Holden N. E., Hopple J. A., Krouse H. R., Lamberty A., Peiser H. S., R v sz K., Rieder S. E., Rosman K. J. R., Roth E., Taylor P. D. P., Vocke R. D., and Xiao Y. K. 2002. Isotope-abundance variations of selected elements—(IUPAC Technical Report). *Pure and Applied Chemistry* 74:1987–2017.
- Dai Z. R., Bradley J. P., Joswiak D. J., Brownlee D. E., Hill H. G. M., and Genge M. J. 2002. Possible in situ formation of meteoritic nanodiamonds in the early solar system. *Nature* 418:157–159.
- Daulton T. L. 2006. Extraterrestrial nanodiamonds in the cosmos. In *Ultrananocrystalline diamond: synthesis, properties, and applications*, edited by Shenderova O. and Gruen D. Norwich, New York: William Andrew Publishers. pp. 23–78.
- Daulton T. L., Eisenhour D. D., Bernatowicz T. J., Lewis R. S., and Buseck P. R. 1996. Genesis of presolar diamonds: Comparative high-resolution transmission electron microscopy study of meteoritic and terrestrial nano-

- diamonds. *Geochimica et Cosmochimica Acta* 60:4853–4872.
- Davis A. M. 2011. Stardust in meteorites. *Proceedings of the National Academy of Sciences* 108:19142–19146.
- De Geuser F., Gault B., Bostel A., and Vurpillot F. 2007. Correlated field evaporation as seen by atom probe tomography. *Surface Science* 601:536–543.
- Elam J. W., Libera J. A., Pellin M. J., Zinovev A. V., Greene J. P., and Nolen J. A. 2006. Atomic layer deposition of W on nanoporous carbon aerogels. *Applied Physics Letters* 89:053124 3 pp.
- Gault B., Moody M. P., Cairney J. M., and Ringer S. P. 2012. *Atom probe microscopy*. New York: Springer. pp. 45–47.
- Greiner N. R., Phillips D. S., Johnson J. D., and Volk F. 1988. Diamonds in detonation soot. *Nature* 333:440–442.
- Heck P. R., Pellin M. J., Davis A. M., Martin I., Renaud L., Benbalagh R., Isheim D., Seidmann D. N., Hiller J., Stephan T., Lewis R. S., Savina M. R., Mane A., Elam J., Stadermann F. J., Zhao X., Daulton T. L., and Amari S. 2010. Atom-probe tomographic analyses of presolar silicon carbide grains and meteoritic nanodiamonds—First results on silicon carbide (abstract #2112). 41st Lunar and Planetary Science Conference. CD-ROM.
- Heck P. R., Pellin M. J., Davis A. M., Isheim D., Seidman D. N., Hiller J., Mane A., Elam J., Savina M. R., Auciello O., Stephan T., Stadermann F. J., Lewis J., Zhao X., Daulton T. L., and Floss C. 2011a. Atom-probe tomographic analyses of Allende and synthetic nanodiamonds. LPI Contributions 9096. Houston, Texas: Lunar and Planetary Institute. 1639 p.
- Heck P. R., Pellin M. J., Davis A. M., Isheim D., Seidman D. N., Hiller J., Mane A., Elam J., Savina M. R., Stephan T., Stadermann F. J., Zhao X., Daulton T. L., and Floss C. 2011b. Atom-probe tomography of meteoritic and synthetic nanodiamonds (abstract). *Meteoritics & Planetary Science* 46:A90.
- Heck P. R., Pellin M. J., Davis A. M., Isheim D., Seidman D. N., Hiller J., Mane A., Elam J., Savina M. R., Stephan T., Stadermann F. J., Zhao X., Daulton T. L., Floss C., and Amari S. 2011c. Atom-probe tomographic analyses of meteoritic nanodiamond residue from Allende (abstract #2070). 42nd Lunar and Planetary Science Conference. CD-ROM.
- Heck P. R., Pellin M. J., Davis A. M., Isheim D., Seidman D. N., Hiller J., Mane A., Elam J., Savina M. R., Auciello O., Stephan T., Larson D. J., Lewis J., Floss C., and Daulton T. L. 2012. Atom-probe tomographic analysis: Towards carbon isotope ratios in individual nanodiamonds (abstract #1790). 43rd Lunar and Planetary Science Conference. CD-ROM.
- Huss G. R. and Lewis R. S. 1994. Noble gases in presolar diamonds I: Three distinct components and their implications for diamond origins. *Meteoritics* 29:791–810.
- Hynes K. M. and Gyngard F. 2009. The presolar grain database: <http://presolar.wustl.edu/~pgd> (abstract #1198). 40th Lunar and Planetary Science Conference. CD-ROM.
- Isheim D., Stadermann F. J., Lewis J. B., Floss C., Daulton T. L., Davis A. M., Heck P. R., Pellin M. J., Savina M. R., Seidman D. N., and Stephan T. 2013. Combining atom-probe tomography and focused-ion beam microscopy to study individual presolar meteoritic nanodiamond particles. *Microscopy and Microanalysis* 19 (Suppl 2):CD974–CD975.
- Kelly T. F. and Larson D. J. 2012. Atom probe tomography 2012. *Annual Review of Materials Research* 42:1–31.
- Kelly T. F. and Miller M. K. 2007. Invited review article: Atom probe tomography. *Review of Scientific Instruments* 78:031101 (20 pp).
- Kingham D. R. 1982. The post-ionization of field evaporated ions: A theoretical explanation of multiple charge states. *Surface Science* 116:273–301.
- Kunicki T. C., Beerman D., Geiser B. G., Oltman E., O'Neill R. W., and Larson D. J. 2006. Atom probe data reconstruction, visualization and analysis with the Imago Visualization and Analysis System (IVAS). Proceedings, 19th International Vacuum Nanoelectronics Conference & 50th International Field Emission Symposium. pp. 535–536.
- Larson D. J., Foord D. T., Petford-Long A. K., Liew H., Blamire M. G., Cerezo A., and Smith G. D. W. 1999. Field-ion specimen preparation using focused ion-beam milling. *Ultramicroscopy* 79:287–293.
- Lawrence D., Alvis R., and Olson D. 2008. Specimen preparation for cross-section atom probe analysis. *Microscopy and Microanalysis* 14:1004–1005.
- Lewis R. S., Anders E., Wright I. P., Norris S. J., and Pillinger C. T. 1983. Isotopically anomalous nitrogen in primitive meteorites. *Nature* 305:767–771.
- Lewis R. S., Ming T., Wacker J. F., Anders E., and Steel E. 1987. Interstellar diamonds in meteorites. *Nature* 326:160–162.
- Lewis R. S., Anders E., and Draine B. T. 1989. Properties, detectability and origin of interstellar diamonds in meteorites. *Nature* 339:117–121.
- Lewis R. S., Huss G. R., and Lugmair G. 1991. Finally, Ba & Sr accompanying Xe-HL in diamonds from Allende. Proceedings, 22nd Lunar and Planetary Science Conference. pp. 807–808.
- Lewis J. B., Isheim D., Floss C., Daulton T., Seidman D. N., Heck P. R., Davis A. M., Pellin M. J., Savina M. R., Hiller J., Mane A., Elam J., Auciello O., and Stephan T. 2012. Meteoritic nanodiamond analysis by atom-probe tomography (abstract #2192). 43rd Lunar and Planetary Science Conference. CD-ROM.
- Maas R., Loss R. D., Rosman K. J. R., De Laeter J. R., Lewis R. S., Huss G. R., and Lugmair G. W. 2001. Isotope anomalies in tellurium and palladium from Allende nanodiamonds. *Meteoritics & Planetary Science* 36:849–858.
- Marquis E. A. and Hyde J. M. 2010. Applications of atom-probe tomography to the characterisation of solute behaviours. *Materials Science and Engineering R* 69:37–62.
- Marty B., Chaussidon M., Wiens R. C., Jurewicz A. J. G., and Burnett D. S. 2011. A ¹⁵N-poor isotopic composition for the solar system as shown by Genesis solar wind samples. *Science* 332:1533–1536.
- Miller M. K. and Hetherington M. G. 1991. Local magnification effects in the atom probe. *Surface Science* 246:442–449.
- Müller E. W., Panitz J. A., and McLane S. B. 1968. The atom-probe field ion microscope. *Review of Scientific Instruments* 39:83–86.
- Owen T., Mahaffy P. R., Niemann H. B., Atreya S., and Wong M. 2001. Protosolar nitrogen. *The Astrophysical Journal* 553:L77–L79.
- Richter S., Ott U., and Begemann F. 1998. Tellurium in presolar diamonds as an indicator for rapid separation of supernova ejecta. *Nature* 391:261–263.

- Russell S. R., Arden J. W., and Pillinger C. T. 1996. A carbon and nitrogen isotope study of diamond from primitive chondrites. *Meteoritics & Planetary Science* 31:343–355.
- Scheinfein M. R. and Seidman D. N. 1993. Time aberrations of uniform fields: An improved reflectron mass spectrometer for an atom-probe field-ion microscope. *Review of Scientific Instruments* 64:3126–3131.
- Seidman D. N. 2007. Three-dimensional atom-probe tomography: Advances and applications. *Annual Review of Materials Research* 37:127–158.
- Seidman D. N. and Stiller K. 2009. An atom-probe tomography primer. *MRS Bulletin* 34:717–724.
- Southworth H. N. and Ralph B. 1969. Image formation from alloys in the field-ion microscope. *Journal of Microscopy* 90:167–197.
- Stadermann F. J., Zhao X., Daulton T. L., Isheim D., Seidman D. N., Heck P. R., Pellin M. J., Savina M. R., Davis A. M., Stephan T., Lewis R. S., and Amari S. 2010. Atom-probe tomographic study of the three-dimensional structure of presolar silicon carbide and nanodiamonds at atomic resolution (abstract #2134). 41st Lunar and Planetary Science Conference. CD-ROM.
- Stadermann F. J., Isheim D., Zhao X., Daulton T. L., Floss C., Seidman D. N., Heck P. R., Pellin M. J., Savina M. R., Hiller J., Mane A., Elam J., Davis A. M., Stephan T., and Amari S. 2011. Atom-probe tomographic characterization of meteoritic nanodiamonds and presolar SiC (abstract #1595). 42nd Lunar and Planetary Science Conference. CD-ROM.
- Stroud R. M., Chisholm M. F., Heck P. R., Alexander C. M. O'D., and Nittler L. R. 2011. Supernova shock-wave-induced CO-formation of glassy carbon and nanodiamond. *The Astrophysical Journal* 738:L27 (5 pp).
- Swart P. K., Grady M. M., Pillinger C. T., Lewis R. S., and Anders E. 1983. Interstellar carbon in meteorites. *Science* 220:406–410.
- Thompson K., Larson D. J., and Ulfig R. 2005. Pre-sharpened and flat-top microtip coupons: A quantitative comparison for atom-probe analysis studies. *Microscopy and Microanalysis* 11:882–883.
- Tsong T. T. 1978. Measurement of the field evaporation rate of several transition metals. *Journal of Physics. F: Metal Physics* 8:1349–1352.
- Virag A., Zinner E., Lewis R. S., and Tang M. 1989. Isotopic Compositions of H, C, and N in C δ Diamonds from the Allende and Murray carbonaceous chondrites (abstract). 20th Lunar and Planetary Science Conference. p. 1158.
- Zinner E. 2007. Presolar grains. In *Meteorites, comets, and planets*, edited by Holland H. D. and Turekian K. K. Treatise on Geochemistry, 2nd ed., vol. 1. Oxford: Elsevier. pp. 1–33.
-